Nonlinear Evolution of Broad-Bandwidth, Laser-Imprinted Nonuniformities in Planar Targets Accelerated by 351-nm Laser Light

In an inertial confinement fusion (ICF) implosion, the target is hydrodynamically unstable, and, as a result, mass modulations in the target (either existing or created by the drive) can grow sufficiently large to disrupt the implosion, reducing its thermonuclear yield.[1] In direct-drive ICF, the nonuniformities in the drive laser can create mass modulations in the target by a process called laser imprinting. It is, therefore, important to understand the evolution of three-dimensional (3-D) broadband initial spectra produced by laser imprinting. Target designs[2,3] rely on the saturation of unstable growth of these broadband spectra by nonlinear effects (predicted by Haan's model[4]), so it is critical to the success of ICF that this saturation be measured and understood.

The linear growth of the Rayleigh–Taylor (RT) instability has been extensively studied in planar targets accelerated by direct drive (laser irradiation).[5–8] These experiments, generally performed with preimposed two-dimensional (2-D) sinusoidal perturbations, were well simulated by hydrocodes, providing confidence that both the energy coupling and the amount of unstable growth are well modeled. The experiments discussed in this article are closely related to those that measure the growth of preimposed mass perturbations.[5,8] The latter provide a baseline calibration for various hydrodynamic effects that occur in the broadband imprinting experiments.

Nonlinear effects are inherent and very important to the evolution of broadband spectra. Several works[9–13] that used laser imprint as the initial perturbation for RT growth have shown the nonlinear evolution of broadband imprinted features. Because of the complexity of nonlinear physics, however, only a qualitative analysis of broadband saturation was shown.[9–13] In recent years several models have been developed to explain nonlinear RT evolution in Fourier[4,14–18] and real space.[17] Multimode nonlinear behavior has been measured in indirect-drive RT experiments with preimposed 3-D, multimode initial perturbations in planar targets.[19,20]

Recent work has shown experimentally[21] that three-dimensional broadband imprinted features exhibit growth that saturates at amplitudes consistent with Haan's model.[4] Here we extended that work to provide a more-detailed analysis of the RT nonlinear evolution of the broadband spectra seeded by laser nonuniformities. In our experiments we used predominantly 20-μm-thick CH targets, which closely resemble the target shells typically used on OMEGA spherical implosions. On OMEGA,[22] the planar targets were accelerated by 351-nm laser beams. Various experiments were performed by different beam-smoothing techniques including distributed phase plates (DPP's),[23] smoothing by spectral dispersion (SSD),[24] and distributed polarization rotators (DPR's).[9,10] Through-foil x-ray radiography was used to measure mass modulations created in planar targets as a result of imprinting and subsequent growth.[25,26] Experimental data are compared with predictions of the Haan model for the evolution of broadband perturbation spectra. The limitations of RT growth by finite target thickness and target "bowing" due to decreased drive toward target edges are also discussed in this article.

It should be noted that the RT instability studied here exists primarily at the ablation surface, the point where the steep temperature front meets the cold overdense material of the shocked target. Perturbations in the target result from both mass modulations (ripples at the ablation surface) and density modulations produced in the bulk of the target. The latter are created primarily by the propagation of nonuniform shocks[5,27,28] produced by intensity nonuniformities in the laser drive that modulate the drive pressure. Through-foil radiographic systems are sensitive to the density–thickness product (optical depth) of the target and, as such, cannot distinguish between mass and density modulations.[5,8] After about 1 ns of acceleration in these experiments, the variations in optical depth produced by the nonuniform shocks become negligible compared to those produced by the ablation-front amplitude. At this point, it is reasonable to ascribe most of the modulation in measured optical depth to the amplitude of the perturbations at the ablation surface.[5]

The next four sections of this article describe experimental configuration, Haan's model for nonlinear saturation of broad-

band nonuniformities, data analysis techniques, and measurements of saturation levels for broadband spectra. The last four sections discuss late-time evolution of broadband spectra, target bowing, limitations of RT growth by finite target-thickness effects, and, finally, results.

Experimental Configuration

Initially smooth, 20- and 40-μm-thick CH targets (ρ = 1.05 g/cm^2) were irradiated at 2×10^{14} W/cm^2 in 3-ns square pulses by five overlapping UV beams (see Fig. 79.40). All five beams had distributed phase plates (DPP's)[23] to enhance the on-target uniformity. Each of the drive beams was focused to a ~900-μm-diam spot size (at the 5% intensity contour) with an on-target intensity distribution measured to be $I \sim \exp\left[-\left(r/r_0\right)^4\right]$.[8] The energy per beam delivered on a target was ~400 J. For some shots SSD[24] and DPR's[9,10] were used. The 2-D SSD had IR bandwidths of 1.25 Å × 1.75 Å producing a 0.25-THz bandwidth at 351 nm. The resultant, five-beam overlapped spot (time integrated) had a constant-intensity region of ~600-μm diameter. The experiments were conducted with three different configurations of beam-smoothing techniques: (1) with DPP's, (2) with DPP's and SSD, and (3) with DPP's, SSD, and DPR's. The on-target uniformity for these cases can be estimated by dividing the time-integrated, single-beam nonuniformities (98%, 8.5%, and 6%) by the square root of 5 (for five beams), yielding 44%, 3.8%, and 2.7%, respectively, for the three configurations.[9,10] The targets were backlit with x rays produced by a uranium backlighter located 9 mm from the driven target and irradiated at ~1×10^{14} W/cm^2 (using 12 additional beams). X rays transmitted through the target and a 3-μm-thick aluminum blast shield (located between the backlighter and drive foils) were imaged by 8-μm pinholes on an x-ray framing camera filtered with 6 μm of aluminum. This yielded the highest sensitivity for an average photon energy of ~1.3 keV. The distance between the target and the pinhole array was 2.9 cm, and the distance between the pinhole array and the framing camera was 35 cm, resulting in a magnification of ~12. The framing camera produced eight temporally displaced images, each of ~80-ps duration. The use of optical fiducial pulses coupled with an electronic monitor of the framing camera output produced a frame-timing precision of ~70 ps. The framing camera images were captured on Kodak T-Max 3200 film, which was digitized with a Perkin-Elmer PDS microdensitometer with a 20-μm-square scanning aperture. The measured target optical depth is the natural logarithm of the intensity-converted images of a target.

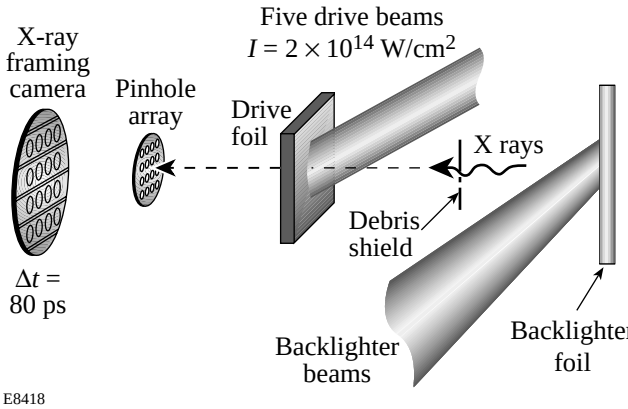

Figure 79.40
Experimental configuration. Five overlapped beams drive a 20-μm-thick CH foil. An additional 12 beams produce x rays from a uranium backlighter foil. X rays traverse the target and are imaged by a pinhole array on a framing camera.

The experiment involved multiple shots where radiographs were obtained at different times. For each shot, up to six images of the same area (400 μm square) of the target (found by the cross-correlation method described later in this article) were analyzed. These images were acquired in time intervals 1.0 to 2.8 ns after the beginning of the drive. The backlighter shape was removed by subtracting a fourth-order, two-dimensional envelope fit to data. The resulting images were the measured modulations of optical depth $D_m(\mathbf{f})$. Using the measured system resolution, noise, and sensitivity, we applied a Wiener filter to reduce noise and deconvolved the system's modulation transfer function (MTF) to recover the target's areal-density modulations $D_t(\mathbf{f})$.[26] The noise in these measurements was dominated by photon statistics of the backlighter x rays, and the system resolution was limited by an 8-μm pinhole.[26]

The primary objective of this experiment is to recover the amplitude of the perturbation at the ablation surface using the measured optical-depth modulations. To do this rigorously requires significant effort. One approach is to use computer simulations of the experiment and detection system to quantify the relationship between modulations in the radiographs and perturbations in the target.[29] Since three-dimensional simulations of laser-imprinted perturbations are difficult, it is advantageous to obtain this relationship experimentally. We simplify the latter process by establishing several reasonable assumptions about the detection system. First, as a result of Al filters, a relatively narrow band ($\Delta E \simeq 200$ eV) of x rays around 1.3 keV is used for radiography. Around 3.5 keV (uranium M-band emission) the spectral component's effect on system

sensitivity and resolution was measured and calculated to be negligible.[26] Second, the backlighter spectrum and filter transmission remain constant during the measurement. Third, the backlighter is produced by 12 beams with phase plates, resulting in a very uniform and predictable backlighter shape. Fourth, there is little heating of the solid part of the target; therefore, the mass absorption coefficient μ is constant in time. Fifth, the amplitudes of the growing imprinted features are large enough that the propagation of a nonuniform shock has little effect on the total optical depth of the target.[5] Given these assumptions, the measured optical depth and the optical depth of the target (areal density) are linearly related as

$$D_m(\mathbf{r},t) = \int d\mathbf{r}' R_{\text{sys}}(\mathbf{r}-\mathbf{r}') D_t(\mathbf{r}',t), \tag{1}$$

where R_{sys} is the point spread function (PSF) of the entire system. The latter is the convolution of the PSF's of the pinhole, the framing camera, the film, and the digitizing aperture of the densitometer. In frequency space, the total system modulation transfer function (MTF) is the product of the MTF's of each of these components. Equation (1) has been derived assuming that the amplitude of the target's optical-depth modulations is small compared to unity. Since Eq. (1) is a linear approximation, it does not treat the generation of harmonics and coupling of modes produced by nonlinearities in the detection system. We have simulated these nonlinearities for modulation amplitudes greater than those measured routinely in our experiments and found that nonlinear effects were negligible compared to the noise in the system. This knowledge was used to create a Weiner filter that uses a linear approximation to the detection system in order to recover the target areal-density modulations.[26]

As an example, Fig. 79.41 shows a fully processed image of the target optical depth at 2.4 ns for a shot with all of the laser-smoothing techniques (DPP's, SSD, and DPR's) employed. The range of 3.6 OD corresponds to a target areal-density (ρR) modulation of about 3.6×10^{-3} g/cm^2. For comparison, the areal density (ρR) of the undriven target is about 2×10^{-3} g/cm^2.

At early times, the contribution to areal-density modulations in the bulk of a target, produced by the propagation of nonuniform shocks, is comparable to those from amplitude modulation at the ablation surface.[5] After ~1 ns of drive, however, the ablation-front modulations with spatial frequencies in the region 10 to 100 mm^{-1} (where measurements are performed) experience sufficient RT growth to dominate any density modulation produced by nonuniform shocks. Thus, at times >1 ns, the amplitude at the ablation surface is well represented by measured modulations.

Once the modulation in target optical depth $D_t(\mathbf{r},t)$ is obtained, the perturbation amplitude in the target $\xi(\mathbf{r},t)$ can be found using spectrally weighted attenuation length λ_{CH},[26] which is inversely proportional to the mass absorption coefficient and the target density:

$$\xi(\mathbf{r},t) = D_t(\mathbf{r},t)\,\lambda_{\text{CH}}. \tag{2}$$

λ_{CH} can be constructed using the target compression C_p calculated by 1-D hydrocode *LILAC*[30] and the measured attenuation length λ_x of the undriven target:

$$\lambda_{\text{CH}} = \frac{\lambda_x}{C_p}. \tag{3}$$

This relation can be used as long as the driven target maintains the cold value of its mass absorption coefficient. Typically, during our experiments the calculated target temperature ($T < 10$ eV) is far below the values that could change the mass absorption coefficient to ~1-keV x rays. λ_x was measured by radiographing undriven, 20-μm-thick CH targets that had

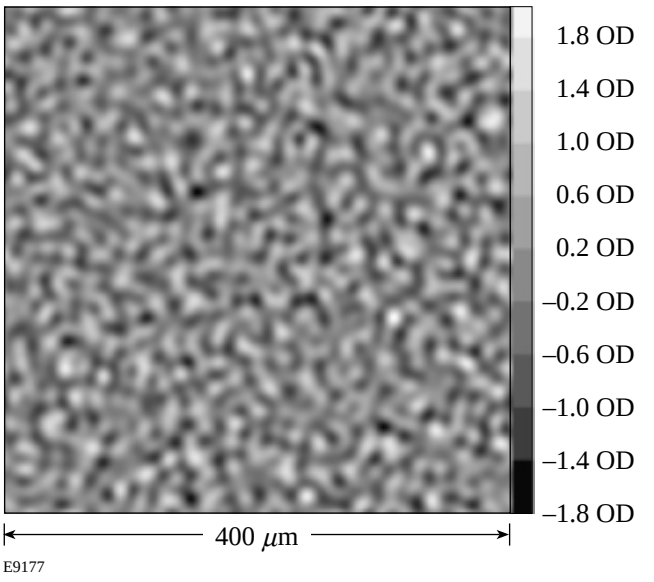

Figure 79.41
Fully processed image of the target optical depth (OD) perturbations captured at 2.4 ns for one of the six shots with all smoothing techniques including DPP's, SSD, and DPR's.

preimposed, low-amplitude (0.5-μm) sinusoidal modulations with wavelengths of 60 and 30 μm. Using these modulations as control references, λ_x was determined to be 10±2 μm. These experiments also showed that both backlighter spectrum and filter transmission remained constant during the measurements.

Haan's Model for Broadband Spectra

In the linear regime of the RT instability, individual modes do not interact and therefore grow exponentially at rates determined by the dispersion relation[31–33]

$$\gamma = \alpha\sqrt{\frac{kg}{1+L_m k}} - \beta k V_a , \tag{4}$$

where γ is the instability growth rate, k is the wave number of the perturbed mode, g is the target acceleration, L_m is the minimum density-gradient scale length, and V_a is the ablation velocity. For CH targets L_m ~1 μm and the constants have values of $\alpha \sim 1$ and $\beta \sim 1.7$. Equation (4) determines how the actual growth rate differs from the classical rate $\gamma \sim \sqrt{kg}$ as a result of density scale length and ablation. For a single-mode initial perturbation, nonlinear effects cause the exponential growth of the mode to saturate at an amplitude $\xi_k \simeq 0.1\,\lambda$ and to subsequently grow linearly in time.[4] Harmonics of the fundamental mode are generated by mode coupling[14] during the exponential growth (in linear phase), leading to the formation of bubbles (penetration of lighter fluid into heavier) and spikes (penetration of heavier fluid into lighter).

The evolution of 3-D broadband perturbations is more complicated. The fastest-growing modes rapidly drive harmonics and coupled modes. The contribution of the mode coupling becomes comparable to the exponential growth for some of the modes, even at small (in the linear regime) amplitudes. As a result, some modes grow faster than others, while some shrink and change their phase;[18] however, the average amplitude of all of the modes at a given spatial frequency grows exponentially at a rate given by Eq. (4).[4,14] Saturation occurs due to the collective behavior of modes because adjacent modes can constructively interfere to create local structures with amplitudes much larger than those of individual modes. As these features experience saturation, the individual modes saturate at amplitudes much less than 0.1 λ. After reaching this saturation level, the modes grow, on average, linearly in time. The transition from the linear (exponential growth) to the nonlinear stage (linear growth) is continuous. Haan formulated a model[4] for the saturation of a 3-D broadband spectrum and found a saturation level of the azimuthally averaged amplitude given by[15,16]

$$S(k) = 2/Lk^2 , \tag{5}$$

where L is the size of the analysis box. The L dependence occurs because the individual Fourier amplitudes of the broadband features depend on the size of analysis region; whereas the rms amplitude $\sigma_{\rm rms}$, a measure of the deviation of the function $\xi(\mathbf{x})$ from its average value $\bar{\xi}$, does not. Using the Fourier transform $\xi(\mathbf{k})$ of the function $\xi(\mathbf{x})$, the rms amplitude $\sigma_{\rm rms}$ is defined as

$$\sigma_{\rm rms} = \sqrt{\sum_k \left|\xi(\mathbf{k})\right|^2 - \left|\xi(\mathbf{k}=0)\right|^2} . \tag{6}$$

The rms amplitude is the physically measurable quantity and therefore must have the same value independent of how it is derived. The number of Fourier modes decreases as the box size is reduced. The nonuniformity's $\sigma_{\rm rms}$ is the square root of the sum of all modes' absolute values squared, as shown by Eq. (6), so the amplitudes of the modes must, concomitantly, increase to keep the nonuniformity's $\sigma_{\rm rms}$ constant.

After it reaches the saturation level $S(k)$, the evolution of the average amplitude $\xi_k(t)$ is given by[4]

$$\xi_k(t) = S(k)\left[1 + \ln\left(\frac{\xi_k^{\rm exp}(t)}{S(k)}\right)\right], \tag{7}$$

where $\xi_k^{\rm exp}(t) = \xi_k(t=0)\exp(\gamma t)$ is the exponential growth in the linear stage of instability. This is equivalent to growth at a constant velocity $V(k)$ in the saturation regime

$$V(k) = S(k)\gamma(k). \tag{8}$$

The behavior predicted by this model is shown in Fig. 79.42 for an initial perturbation spectrum that had constant power per mode as a function of spatial frequency. This is representative of the broadband features imprinted by irradiation nonuniformities that arise primarily from the speckle pattern produced by DPP's and SSD.[34] The evolution of this spectrum (plotted as the average amplitudes versus spatial frequency for seven different times between t = 1.3 to 2.2 ns) is modeled simply by applying the growth-rate dispersion relation [Eq. (4)], the saturation level [Eq. (5)], and the evolution in the saturation regime [Eq. (7)], where the target acceleration g = 50 μm/ns^2, ablation velocity V_a = 2.5 μm/ns, and the

nonuniformity's initial σ_{rms} = 0.09 μm. The amplitudes are converted to target optical depth by dividing by the measured, spectrally weighed, attenuation length λ_x = 10±2 μm and multiplying by the simulated compression of the target (about 2 for 1.5 ns). The simulated target density at the ablation surface is shown in Fig. 79.43. The high-frequency modes grow most rapidly and saturate at the level given by Eq. (5), while the low-frequency modes grow more slowly. As a result, the mid-frequency modes experience the largest growth factors, producing a peak in the spectrum. As the evolution progresses, the mid-frequency modes begin to saturate, and the peak moves to longer wavelengths. This behavior is relatively insensitive to the initial spectrum or drive conditions; therefore, most broad-bandwidth initial spectra will evolve similarly given sufficient time. Variations in growth rates of up to 50%, or in the σ_{rms} of the initial spectrum of up to two orders of magnitude, have little effect on the predicted spectral evolution; the only requirement is that the spectrum be broadband. For example, according to Haan's model the initial perturbation spectrum that has constant Fourier amplitude and σ_{rms} = 0.5 μm undergoes similar evolution to that shown in Fig. 79.42 but it occurs at earlier times (between t = 0.8 to 1.6 ns) if the drive conditions are the same. This behavior has been tested experimentally by varying amplitudes of initial perturbation using a variety of laser-smoothing techniques.

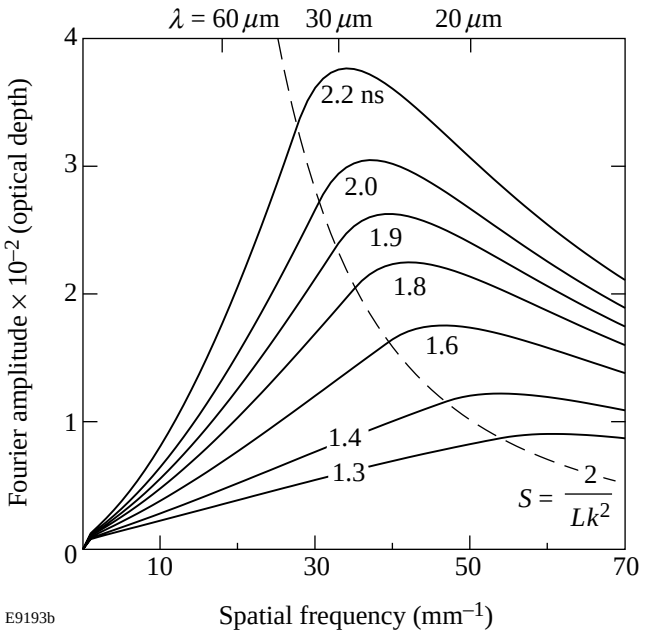

Figure 79.42
Predicted Fourier amplitudes of optical depth using Haan's model for an assumed spectrum of perturbations with initial flat power per mode (σ_{rms} = 0.09 μm) spectrum, target acceleration of g = 50 μm /ns^2, ablation velocity of V_a = 2.5 μm /ns, and L = 400 μm at times 1.3, 1.4, 1.6, 1.8, 1.9, 2.0, and 2.2 ns. Haan's saturation amplitude S is shown by the dashed line.

Image Cross-Correlations

The experiment involves multiple shots with CH targets and with different smoothing techniques applied. For each shot, up to six unfiltered images of the same area of the target, found with a cross-correlation technique, were processed with a 400-μm analysis box. Figure 79.44 shows two images of the target acquired at 2.4 ns and 2.5 ns for a shot with all smoothing techniques employed. The same 400-μm-sq area of the target was found in each of these images when the cross-correlation between the two analysis regions was maximized. The cross-

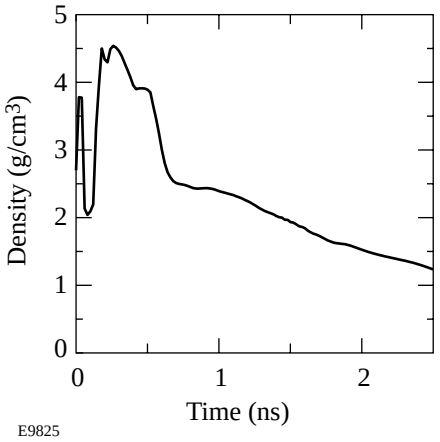

Figure 79.43
Calculated target density at the ablation surface as a function of time.

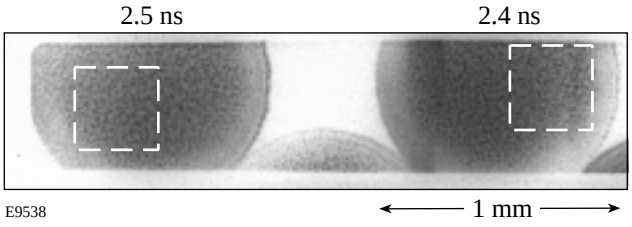

Figure 79.44
Two images of the target acquired at 2.4 ns and 2.5 ns for a shot with all smoothing techniques employed. Two 400-μm-square regions indicated by the square boxes were taken for cross-correlation analysis.

correlation function for two images with target optical depths $D_{t1}(\mathbf{r})$ and $D_{t2}(\mathbf{r})$ is given by

$$C(\mathbf{r}) = \frac{\int d\mathbf{r}' D_{t1}(\mathbf{r}' + \mathbf{r}) D_{t2}(\mathbf{r}')}{\sqrt{\int d\mathbf{r} D_{t1}(\mathbf{r})^2 \int d\mathbf{r} D_{t2}(\mathbf{r})^2}}. \quad (9)$$

If two images of the target are shifted by some distance a, then the maximum of the cross-correlation function $C(\mathbf{r})$ will be shifted by the same distance from the center of coordinates ($\mathbf{r} = 0$), as can be seen from Eq. (9). For example, if two images at 2.4 ns and 2.5 ns are misaligned by $a_x = 133$ μm in horizontal and $a_y = 67$ μm in vertical directions, the peak of the cross-correlation function between these two images is shifted from the center of coordinates by the same distances a_x and a_y as shown in Fig. 79.45(a). When one of the images is moved by the distances a_x and a_y, aligning these two images, the peak of the cross-correlation function moves toward the center of coordinates as shown in Fig. 79.45(b). At the same time, the cross-correlation coefficient between these two images, which is defined as the maximum of $C(\mathbf{r})$, increases from 17% for misaligned images to 34% for aligned images because larger areas of the target overlap for two aligned images.

The details of target nonuniformity structure are unique and specific only to images taken at the same shot. It is therefore expected that the cross-correlation technique should find little correlation between two images taken from different shots. The typical cross-correlation function of two images taken on different shots is shown in Fig. 79.45(c). This function has no

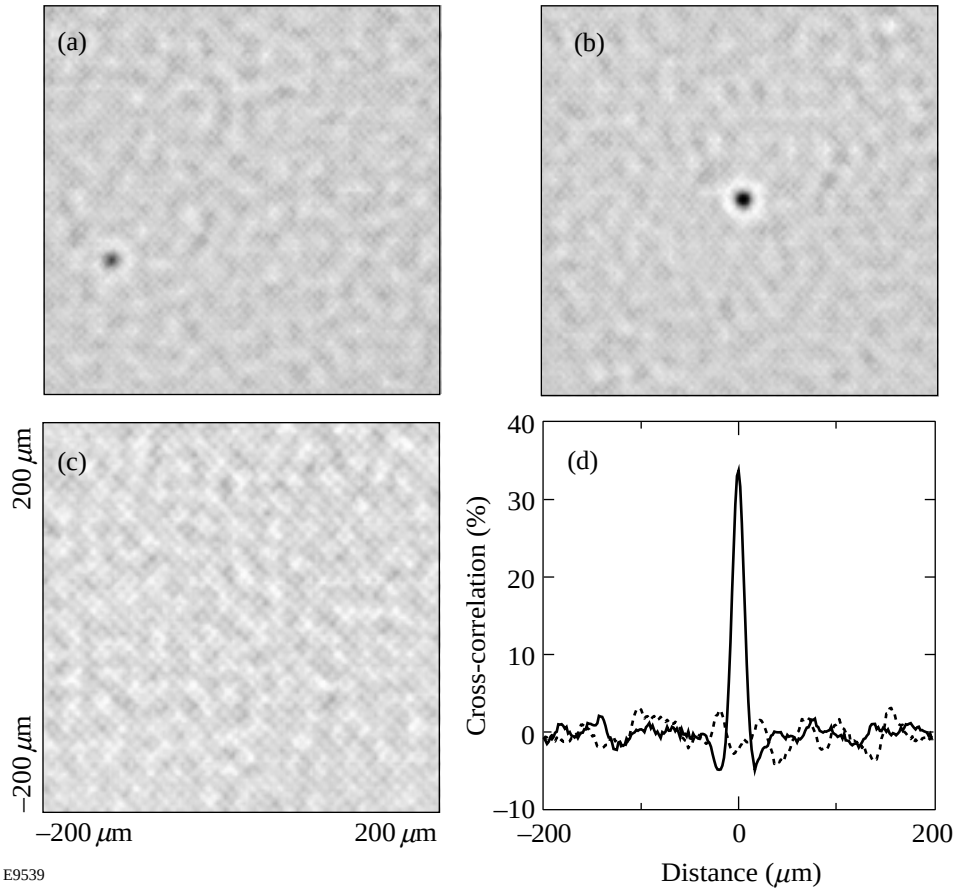

Figure 79.45
The cross-correlation function between two images. (a) Two images are shifted by 133 μm in the horizontal direction and 67 μm in the vertical direction, respectively. The cross-correlation coefficient between the two images is 17%. (b) When two images are aligned, the maximum of the cross-correlation function is then located at the center of coordinates at $\mathbf{r} = 0$. The cross-correlation coefficient between the two images increases to 34%. (c) The cross-correlation function between the two images taken on different shots showing little correlation. (d) The lineout through the center of coordinates of the cross-correlation function shown in (c) for two images taken at different shots (dashed line). The lineout through the center of coordinates of the cross-correlation function shown in (b) for 2.4-ns and 2.5-ns images taken during the same shot (solid line).

pronounced peaks; it fluctuates around zero, as shown by the dashed line in Fig. 79.45(d), which is the lineout of this function through the center of coordinates. This indicates that there is no correlation between features in images from different shots. In contrast, images taken on the same shot (such as those acquired at 2.4 and 2.5 ns and shown in Fig. 79.44) are well correlated. This is shown by the lineout through the center of their cross-correlation function as shown in Fig. 79.45(d) by the solid line. The cross-correlation between images greatly increased after they were Wiener filtered: for example, the cross-correlation coefficient between these images increased from 34% to 70%. This indicates that the image processing efficiently reduced the noise in these images. The upper limit of the cross-correlation is determined by the amount of evolution the target perturbations experienced between the times the images were captured.

The accuracy of the image alignment using the cross-correlation technique has been defined in the following way: For a particular shot, five images (A, B, C, D, and E) were aligned with a sixth image (F) by moving the peaks of all five cross-correlation functions toward their centers of coordinates. Then each of the five images was cross-correlated to each other. It was found that the peaks of all these cross-correlation functions were located no farther than 1 pixel (1.67 μm) from the centers determined by the first step. This indicates that the accuracy of the alignment is not worse than 2 μm.

Figure 79.46 shows six fully processed (Wiener-filtered) sub-images (L = 100 μm) of the target optical depth for one of the shots with full smoothing (DPP's, SSD, and DPR's applied) captured at 1.6, 1.9, 2.0, 2.2, 2.4, and 2.5 ns and aligned by the cross-correlation technique. The temporal evolution to longer-scale structures is evident. All images are well correlated indicating that the evolution is of the same features. Figure 79.47 shows the cross-correlation coefficients $C(\mathbf{r}=0)$ between these different images. The solid line shows that the cross-correlation C ($\mathbf{r}$ = 0) of the image at 2.5 ns with itself equals 1 (at 2.5 ns) and its cross-correlation with other images (at other times) decreases as a time separation between images increases. The dashed line in Fig. 79.47 shows the same behavior for the cross-correlation of the image at 2.2 ns with the other images. In fact, the same behavior has been observed for each time frame in all six shots, i.e., the cross-correlation between neighboring images is always higher than with more-distant images, which confirms that the image processing allows an observation of the evolution of the same features of target perturbations.

Nonlinear Saturation of RT Growth

As was pointed out earlier, predictions by the Haan's model for the shape of the late-time spectrum are relatively insensitive to the initial perturbation spectrum; therefore, most broad-bandwidth initial spectra evolve similarly. Variations of up to two orders of magnitude in the initial amplitudes of the spectrum have little effect on the predicted spectral evolution. This prediction has been tested experimentally by varying the amplitudes of initial perturbation using different laser-smoothing techniques. The primary experiment involves multiple shots with planar, 20-μm-thick CH targets taken with different smoothing techniques employed: with DPP's, SSD, and DPR's (six shots), with DPP's and SSD (three shots), and with DPP's only (two shots).

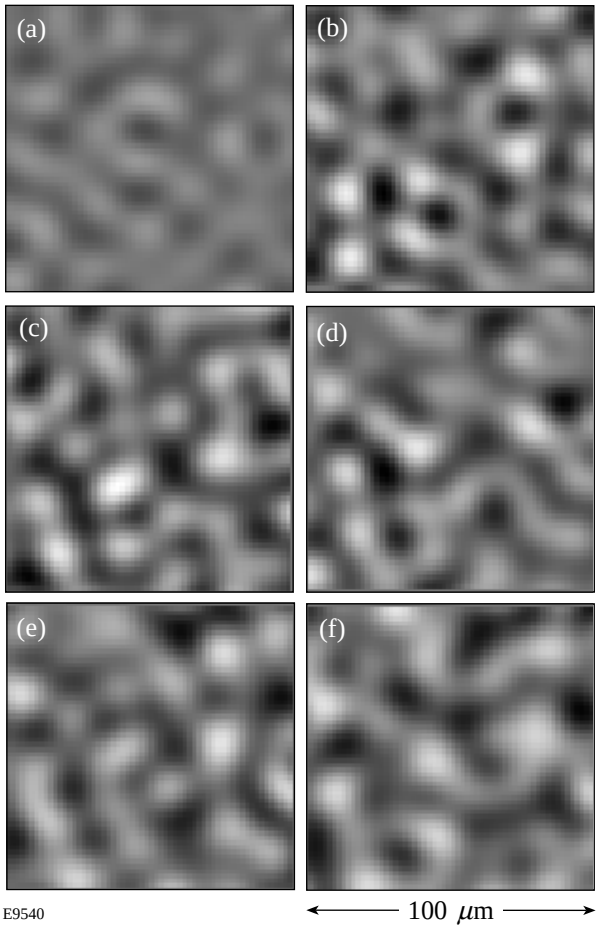

Figure 79.46
Fully processed sub-images (with a box size of 100 μm) of the target optical depth captured at (a) 1.6, (b) 1.9, (c) 2.0, (d) 2.2, (e) 2.4, and (f) 2.5 ns for one of the six shots taken with laser conditions that include DPP's, SSD, and DPR's. The evolution in time to longer-scale structures is evident.

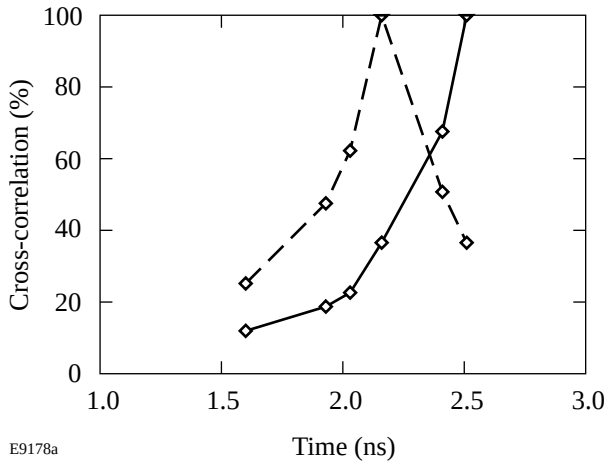

Figure 79.47
Cross-correlation of different time images for one of the six shots taken with laser conditions that include DPP's, SSD, and DPR's. The cross-correlation coefficients of images captured at 2.5 ns and 2.2 ns with all other images are shown by the solid line and the dashed line, respectively.

The evolution of the averaged amplitudes (obtained by azimuthally averaging the Fourier amplitudes at each spatial frequency) of the measured target's optical-depth modulation as a function of spatial frequency with planar, 20-μm-thick CH targets is shown in Fig. 79.48(a) for one shot at times of 1.4 to 2.2 ns and in Fig. 79.48(b) for another shot at somewhat later times of 1.6 to 2.4 ns. In these shots laser beams had full smoothing techniques employed (i.e., DPP's, SSD, and DPR's). Figures 79.48(c) and 79.48(d) show the evolution of nonuniformity spectra for shots with DPP's and SSD for times of 1.6 to 1.9 ns for one shot and of 1.6 to 2.0 ns for the other, and Figs. 79.48(e) and 79.48(f) for shots with DPP's only for times of 1.3 to 1.5 ns for one shot and of 1.6 to 1.8 ns for the other. The initial amplitudes of imprinted perturbations are expected to be higher in shots with less laser uniformity.

One can readily see that the measured spectra are peaked and that the peak shifts toward longer wavelengths as time progresses, similar to the predicted behavior shown in Fig. 79.42. Moreover, the dashed line, which shows the Haan saturation level, is in good agreement with the position of the spectral peak. The saturation level was converted to optical depth using the spectrally weighed attenuation length λ_x and the predicted compression (about 2 at times ~1 to 2 ns). Similar behavior was observed for all shots taken under all drive conditions with different smoothing techniques employed. For the data with less laser uniformity [Figs. 79.48(e) and 79.48(f), DPP's only], the initial imprinted amplitudes are higher, and as a result, the RT evolution is observed earlier in time than in the case with more-uniform drive, which includes SSD and DPR's [Figs. 79.48(a) and 79.48(b)].

Figure 79.48 shows that the measured growth of the amplitudes at 20-μm wavelength is much less pronounced than that of 30 μm for all shots. This is because the amplitudes at 20 μm are predicted to be already above Haan's saturation level at about 0.01 OD, while amplitudes at 30 μm experience a transition from exponential growth to the saturated growth with constant velocity at about 0.022 OD. The amplitude at 60 μm is predicted to be below the saturation level and therefore should grow exponentially during this time interval. To support these assertions, we measured the growth of low-amplitude, preimposed, 2-D, 60-μm-wavelength and 30-μm-wavelength, single-mode, sinusoidal perturbations on 20-μm-thick CH foils driven with the irradiation conditions that included DPP's, SSD, and DPR's. Targets with initial perturbation amplitudes of 0.05 and 0.125 μm at 60-μm wavelength and 0.025 μm at 30-μm wavelength were used. These initial amplitudes are sufficiently low that they are expected to be in the linear regime for at least 2.5 ns, yet have high enough amplitudes that mode coupling from the broadband spectrum has no effect on their evolution. Figure 79.49(a) shows that the broadband features at 60 μm (the combined data from six shots) grow at a similar rate as the preimposed 60-μm modulations (upper data points for two shots). Exponential fits to these data (three solid lines) indicate growth rates of 0.96 $\pm$0.02 ns^{-1} and 1.02$\pm$0.02 ns^{-1} for the preimposed modulations and 0.91$\pm$0.05 ns^{-1} for the broadband modulations. Figure 79.49(b) shows that the broadband features at 30 μm (the combined data from six shots) experience a transition from linear to nonlinear phases at an amplitude of about 0.02 OD, which is 30 times lower than the single-mode saturation value of 0.6 OD (0.1 λ). At the same time, the two preimposed 30-μm modulations (upper data points) grow exponentially with growth rates of 1.45$\pm$0.02 ns^{-1} and 1.54$\pm$0.02 ns^{-1}, respectively. These data clearly show the wavelength-dependent saturation level.

The preimposed 30-μm and 60-μm modulations were fitted with an exponential in order to compare growth rates with those measured for early times[5,8] (see later in the **Finite Target Thickness Effect** section). For broadband modulations, both exponential and polynomial fits have been used to quantify the transition from the exponential to saturated growth. Figure 79.49(b) shows that for broadband modulations at 60 μm, the exponential fit (solid line) closely matches the third-order polynomial fit (dashed line). The standard deviations are 0.0021 OD and 0.0022 OD, respectively. For 30-μm broadband modulations shown in Fig. 79.49(b), however, the expo-

nential (dashed line) does not fit data well (the standard deviation is 0.0039 OD) compared to the polynomial fit (solid line; the standard deviation is 0.0022 OD), which closely follows the saturated evolution of these broadband data.

Figure 79.50 summarizes data from 11 shots performed with (1) DPP's, SSD, and DPR's [six shots, Figs. 79.50(a), 79.50(d), and 79.50(g) for the average broadband amplitudes at wavelengths of 60 μm, 30 μm, and 20 μm, respectively],

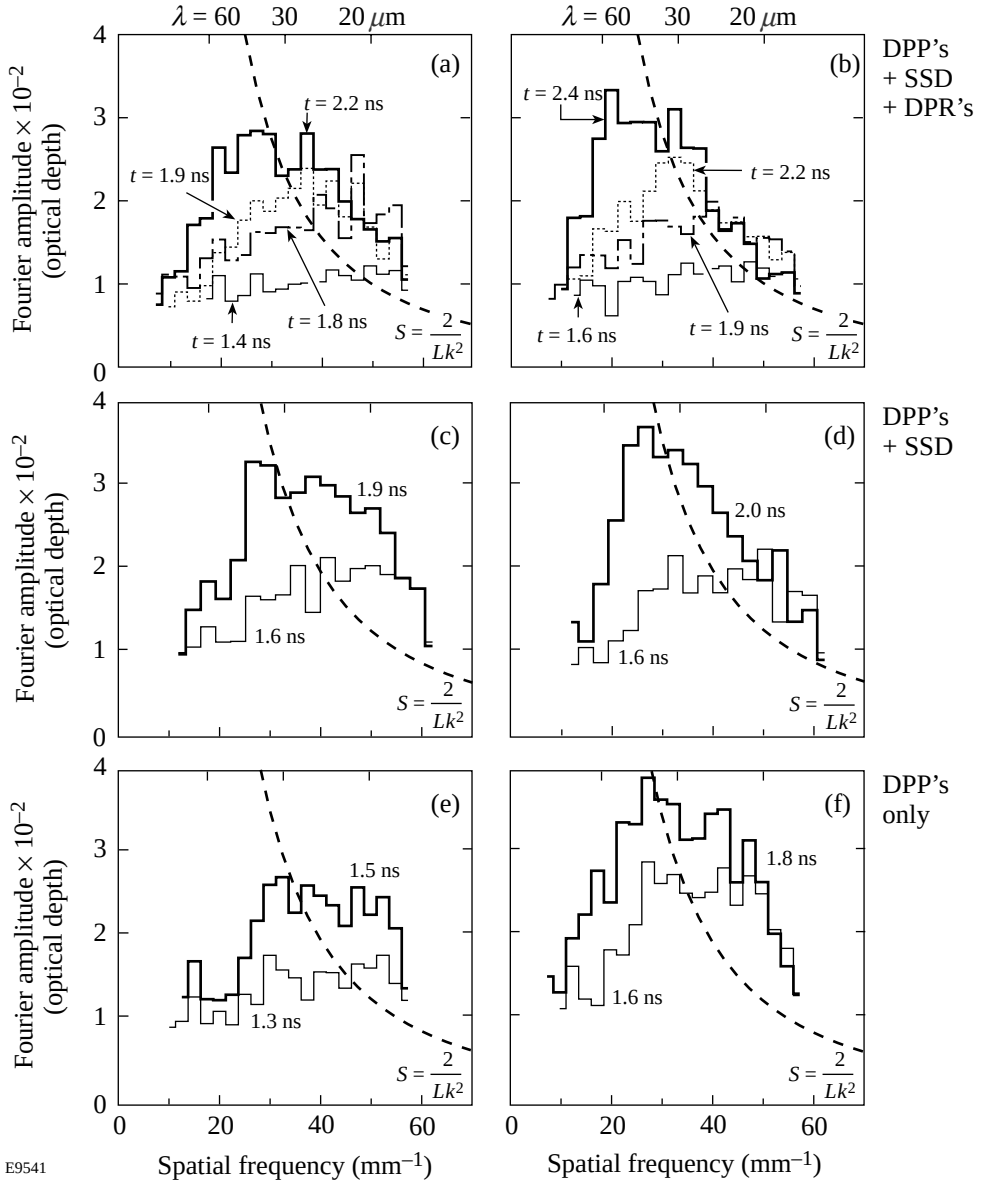

Figure 79.48
The measured azimuthally averaged Fourier amplitudes of the optical-depth modulations as a function of spatial frequency for six shots: (a) a 20-μm-thick foil at times 1.4, 1.8, 1.9, and 2.2 ns with laser conditions that include DPP's, SSD, and DPR's; (b) at 1.6, 1.9, 2.2, and 2.4 ns with DPP's, SSD, and DPR's; (c) at 1.6 and 1.9 ns with DPP's and SSD; (d) at 1.6 and 2.0 ns with DPP's and SSD; (e) at 1.3 and 1.5 ns with DPP's; and (f) at 1.6 and 1.8 ns with DPP's. Haan's saturation amplitude S is shown by the dashed line.

(2) DPP's and SSD [three shots, Figs. 79.50(b), 79.50(e), and 79.50(h)]; and (3) DPP's only [two shots, Figs. 79.50(c), 79.50(f), and 79.50(i)]. It is expected that SSD smoothes out perturbations at high spatial frequencies much more efficiently than at low spatial frequencies;[34] therefore, the expected initial imprinted spectra with and without SSD have not only different nonuniformities σ_{rms}, but also different shapes. According to Haan's model, however, later in time, and after considerable RT growth, the perturbation spectra are expected to be similar but shifted in time with the evolution occurring later in the case of DPP's plus SSD compared to DPP's only.

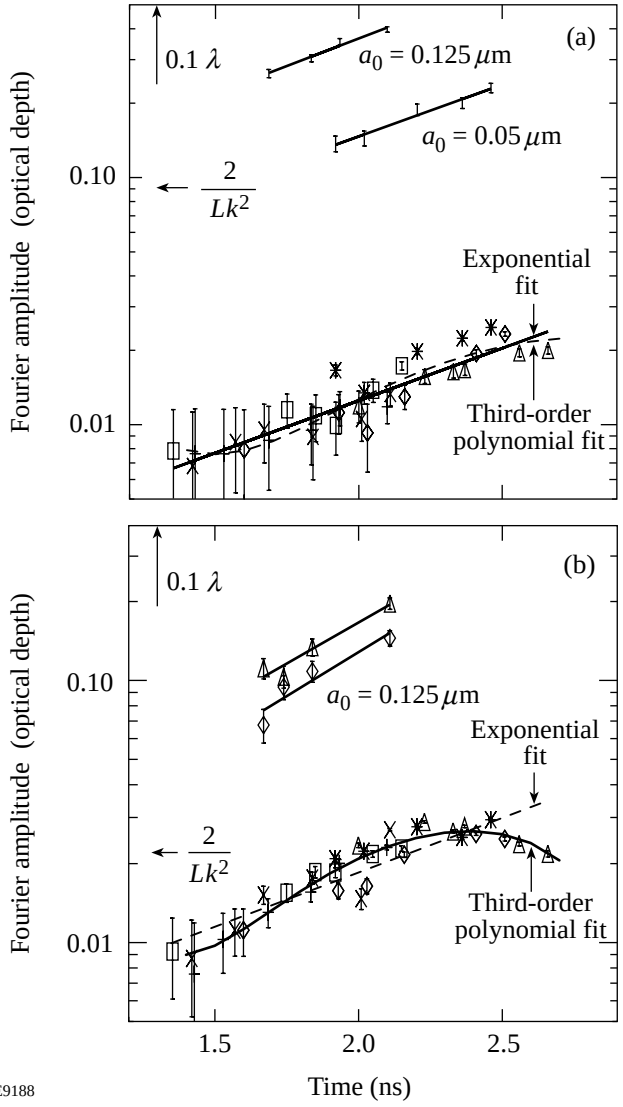

Figure 79.49
(a) Average Fourier amplitudes of optical depth of imprinted features versus time at 60-μm wavelength for six shots (distinguished by different symbols) and the amplitude of preimposed 60-μm perturbations of corrugated targets with initial amplitudes of 0.05 and 0.125 μm (upper data). (b) The same for the 30-μm wavelength with the amplitudes of initial, preimposed, 30-μm perturbations of 0.025 μm (upper data). Exponential fits (solid lines) were used for the preimposed corrugation data, 60-μm imprinted data (solid lines), and 30-μm imprinted data (dashed line), and a third-order polynomial fit was used to the imprinted data at 60 μm (dashed line) and 30 μm (solid line).

The measured temporal evolution for all three cases is similar, as evident from the evolution of the amplitudes of broadband perturbations at 60-μm, 30-μm, and 20-μm wavelengths. The 30-μm- and 20-μm-wavelength perturbations saturate at different times for different smoothing conditions but always at the same levels. The 60-μm perturbations grow in the linear regime (exponential growth) with similar growth rates (0.70±0.05 ns^{-1}, 0.93±0.05 ns^{-1}, and 0.91±0.05 ns^{-1} with DPP's only; DPP's and SSD; and DPP's, SSD, and DPR's, respectively, for all smoothing conditions). As shown earlier, these growth rates are in very good agreement with the measured growth rates of preimposed 2-D sinusoidal perturbations at a 60-μm wavelength [Fig. 79.49(a), upper data points].

For cases with less laser uniformity [case (3): DPP's only], the initial imprinted amplitudes are higher, and as a result, the RT evolution is advanced in time [~250 ps earlier than in case (2), and ~500 ps earlier than in case (1)]. This observation is evident for the 60-μm, 30-μm, and 20-μm wavelengths of broadband perturbations. Note also that the 30-μm-wavelength perturbations saturate at higher amplitude than the 20-μm perturbations, as expected.

Even though the experimental data (see Fig. 79.48) cannot show the saturation level $S(k) = 2/Lk^2$ explicitly, it was tested by comparing peaks of measured Fourier spectra with those predicted by using Haan's model. Such comparison becomes possible because the shape of Fourier spectra and the position of their peaks depend primarily on the saturation level rather than on the initial or drive conditions (shown experimentally in Fig. 79.48). For example, from Fig. 79.48(a) one can see that measured spectral peaks at spatial frequencies of 30 mm^{-1} and 50 mm^{-1} are positioned at the values of Fourier amplitudes of approximately 2.7×10^{-2} and 1.2×10^{-2} OD, at times 2.2 ns and 1.4 ns, respectively. The predicted spectral peaks at these spatial frequencies are at the values of approximately 3.7×10^{-2} and 1.2×10^{-2} OD, respectively, as shown in Fig. 79.42.

The main experimental errors in measurements of target optical depth shown in Fig. 79.48 include noise in the experimental system (dominated by photon statistics of the backlighter x rays), uncertainty of the system resolution, and nonlinearities

in the detection system, which was considered to be linear during Wiener filtering and MTF deconvolution.[26] The total uncertainty of optical-depth measurements at the spatial frequency range of 30 to 50 mm^{-1} was determined to be about 10^{-3} OD. It included the relative error of system resolution measurement, which was about 4%, and the uncertainty due to nonlinearity in the detection system, which was about 2% of the noise in the experimental system.[26]

The Haan's model predictions shown in Fig. 79.42 were converted to the optical depth using spectrally weighted attenuation length λ_{CH},[26] which depends on the calculated target compression C_p and the measured attenuation length λ_x of the undriven target [see Eq. (3)]. λ_x was determined to be 10±2 μm,[26] and the target compression was calculated to be about $C_p = 1.7 \pm 0.3$ during the time interval of 1.4 to 2.2 ns.

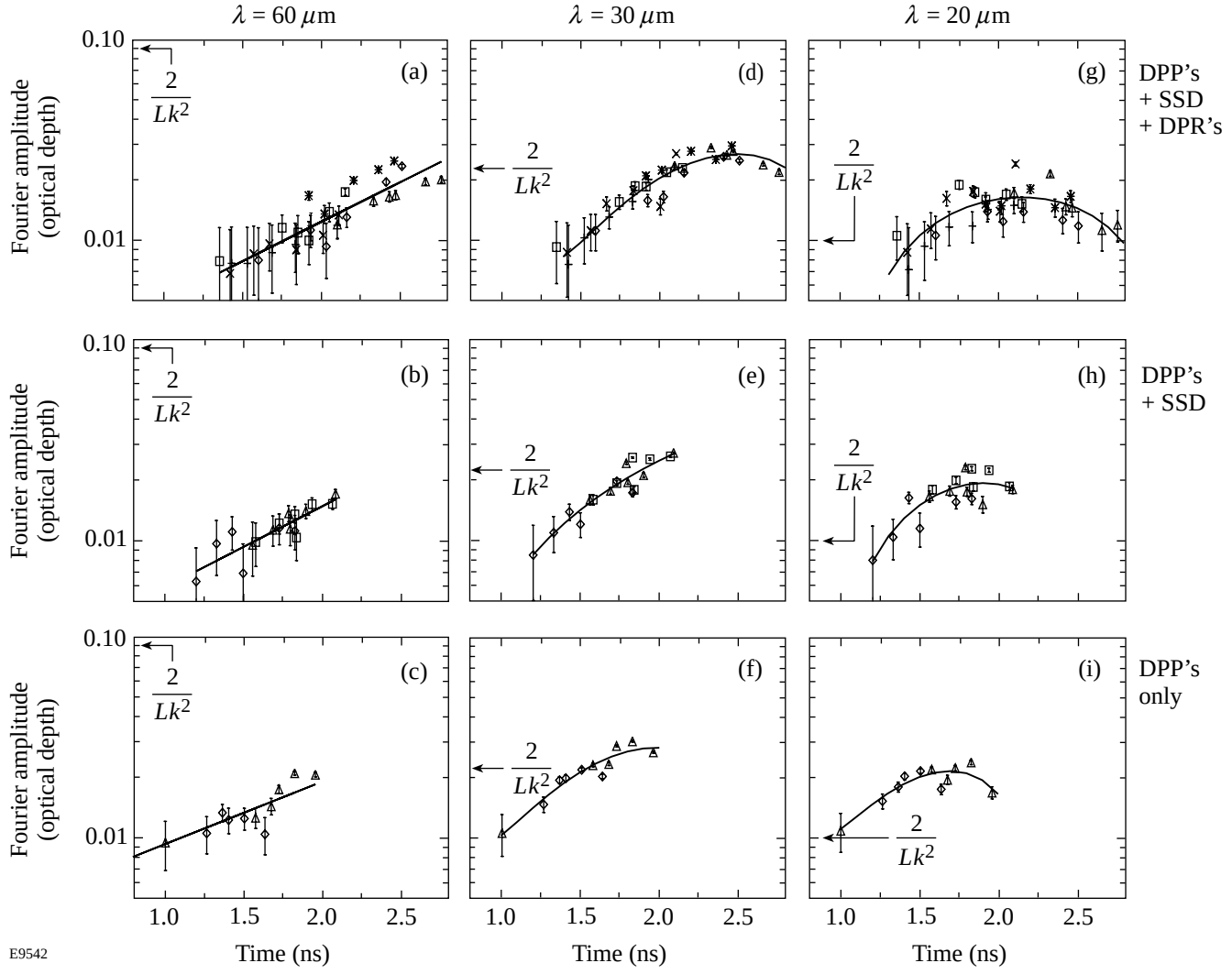

Figure 79.50

(a) Average Fourier amplitudes of optical depth of imprinted features versus time at 60-μm wavelength for six shots (distinguished by different symbols) with DPP's, SSD, and DPR's. Exponential fit (solid line) indicates the growth rate of 0.91±0.05 ns^{-1}. (b) The same for the three shots with DPP's and SSD. Exponential fit (solid line) indicates the growth rate of 0.93±0.05 ns^{-1}. (c) The same for the two shots with DPP's only. Exponential fit (solid line) indicates the growth rate of 0.70±0.05 ns^{-1}. (d) Average Fourier amplitudes of optical depth of imprinted features versus time at 30-μm wavelength for six shots with DPP's, SSD, and DPR's. The solid line is a third-order polynomial fit. (e) The same for the three shots with DPP's and SSD. (f) The same for the two shots with DPP's only. (g) Average Fourier amplitudes of optical depth of imprinted features versus time at 20-μm wavelength for six shots with DPP's, SSD, and DPR's. The solid line is a third-order polynomial fit. (h) The same for the three shots with DPP's and SSD. (i) The same for the two shots with DPP's only.

Using all of these uncertainties, the measured amplitudes of optical-depth modulations that have been converted to perturbation amplitudes in the target [using Eq. (2)] are $15.9 \times 10^{-2} \pm 4.5 \times 10^{-2}$ μm and $7.1 \times 10^{-2} \pm 1.6 \times 10^{-2}$ μm at spatial frequencies of 30 mm^{-1} and 50 mm^{-1}, respectively. Those predicted by Haan's model are 18×10^{-2} μm and 6.0×10^{-2} μm at spatial frequencies of 30 mm^{-1} and 50 mm^{-1}, respectively.

To demonstrate the agreement of these data with the Haan's model, we have compared the measurements and the predictions for the peak of the nonuniformity spectrum in accelerated targets. As has been discussed, the location of the peak follows the predicted trend to longer wavelengths, but it is important to compare the actual amplitude of that peak. Since that amplitude is independent of the initial conditions, we are able to plot together all data shown in Fig. 79.48, irrespective of the different laser-uniformity conditions. Again, the amplitude is obtained using the measured attenuation length of the undriven target and the calculated target compression (Fig. 79.43 shows the density as a function of time). In Fig. 79.51, the amplitudes at which the peaks in the measured spectra occur are plotted versus those for the predicted spectra. These data show that the Haan's model well represents the spectral peaks of broadband nonuniformities.

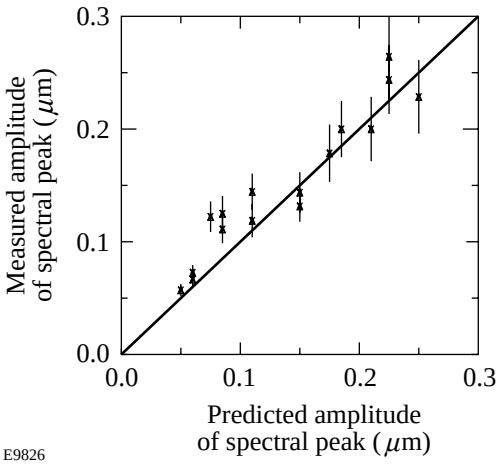

Figure 79.51
The amplitude of measured spectral peak as a function of predicted spectral peak.

In summary, broad-bandwidth perturbations were observed to saturate at levels predicted by Haan's model,[4] which were much lower than the single-mode saturation levels (0.1 λ). This has been shown by the combined data from shots having different drive uniformities. This behavior was noted in both the shape of the spatial Fourier spectra and the temporal behavior of modes at various wavelengths. In addition, it was found that the growth of 3-D perturbations from the broadband spectrum in the linear regime is the same as that for the linear growth of preimposed 2-D perturbations, also in agreement with Haan's model. The measured spectral evolution including the saturation level is insensitive to the details of the initial perturbation spectrum; this is also in agreement with Haan's model.

The relationship between the evolution of the preimposed modes and their coupling to the broadband spectrum must be clarified. The results inferred from Fig. 79.49 require that the growth of the preimposed modes remain in the linear regime (exponential growth) and unaffected by mode coupling. It was experimentally observed that the absolute values of Fourier amplitudes of the broadband spectra are randomly distributed from zero to about twice the average level $2\bar{\xi}_k(t)$ for any azimuthal lineout with wave vector k and at any time t. Therefore, the evolution of any mode $\xi_k(t)$ from the azimuthal lineout at a wave vector k of the broadband spectrum is confined between zero and $2\bar{\xi}_k(t)$. This means that the effects of nonlinear mode coupling on any particular mode $\xi_k(t)$ from all other modes is of the order of $\bar{\xi}_k(t)$ or less. This observation is in agreement with the theoretical work performed by Haan[14] for ablatively accelerated targets. If the amplitude of some particular mode $\xi_k(t)$, growing in the linear regime, is much higher than the average level of broadband spectrum $\xi_k(t) >> \bar{\xi}_k(t)$ as for the preimposed modes from Fig. 79.49, then nonlinear effects will be only a small fraction of its amplitude $\xi_k(t)$. For example, the evolution of the mode $\xi_k(t)$ can be approximated to second-order accuracy and neglecting high-order terms by[14]

$$\xi_k(t) = \xi_k^{\exp}(t) + 1/2\, k\left[\sum_{k'} \xi_{k'}^{\exp}(t)\xi_{k+k'}^{\exp}(t) - 1/2 \sum_{k'<k} \xi_{k'}^{\exp}(t)\xi_{k-k'}^{\exp}(t)\right], \quad (10)$$

where $\xi_k^{\exp}(t) = \xi(t=0)\,\exp[\gamma(k)t]$ is the exponential (or first-order) amplitude of mode k. If the amplitude of some particular mode $\xi_k(t)$, growing in the linear regime, is much higher than the average level of broadband spectrum $\xi_k(t) >> \bar{\xi}_k(t)$ as for preimposed modes from Fig. 79.49, then nonlinear effects will be only a small fraction of its amplitude $\xi_k(t)$ [i.e., the first linear term in Eq. (10) is much larger than the second nonlinear term]. This means that the effect of mode coupling on the amplitudes of 60-μm and 30-μm preimposed modes [which are 10 to 20 times above the average level of broadband

amplitudes (see Fig. 79.49)] is small (of the order of 5% to 10% of their amplitudes) and can be neglected compared with their exponential growth in the linear regime.

The same concept can be expected in a simple physical picture. Figure 79.52 schematically shows an image of the driven target that has a single-mode perturbation (dashed lines) and broadband features with individual 3-D bubbles (solid lines). In some small regions (containing only one or two bubbles), the material flow in the horizontal direction can be dominated by the flow from individual 3-D bubbles. In 3-D, the material from bubbles flows in all directions, but it flows only in one horizontal direction from 2-D bubbles. In the whole region of box size L, however, the material flow in the horizontal direction is dominated by the flow from the tips of the 2-D bubble (dashed lines) because the overall contribution to the flow in this direction from the 3-D bubbles becomes much smaller in the whole region with box size L. Therefore, the overall effect of the broadband features on the evolution of a single mode is insignificant providing that the amplitude of the single mode is high enough. This consideration in real space is complimentary to that in Fourier space described in the previous paragraph.

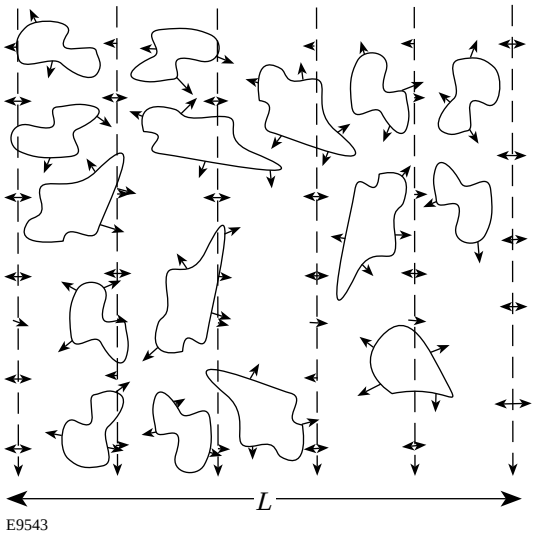

Figure 79.52
Schematic image of the driven target, which has a single-mode perturbation (dashed lines) and broadband features with individual 3-D bubbles (solid lines). In the small regions (containing only one or two bubbles), the material flow in the horizontal direction can be dominated by the flow from individual 3-D bubbles (solid lines). In the whole region with box size L, however, the material flow in the horizontal direction is dominated by the flow from the tips of the 2-D bubble (dashed lines).

Late-Time Perturbation Evolution

In Fig. 79.50, the amplitudes of both the 20-μm- and 30-μm-wavelength broadband perturbations decrease late in time (at 2.5 to 2.8 ns for the case with all smoothing techniques employed). In the nonlinear regime, Haan's model predicts the growth of these perturbations to be linear in time (constant velocity growth) after they reach their saturation levels. This is in contradiction with experimental data. Figure 79.53 shows nonuniformity spectra at 2.5 ns (dashed line) and 2.8 ns (solid line) for one of the shots with all laser-smoothing techniques employed including DPP's, SSD, and DPR's. It clearly shows a decrease in amplitude of all spatial frequencies higher than 30 mm^{-1}. Figure 79.54 shows images of the target at 2.5 ns (a)

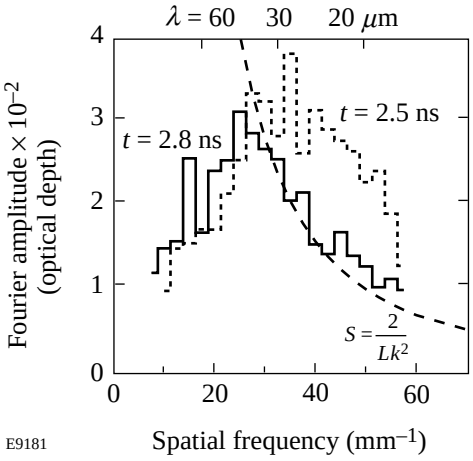

Figure 79.53
Experimentally measured late-time perturbation spectra. Azimuthally averaged Fourier amplitude of the optical-depth modulation as a function of spatial frequency for a 20-μm-thick foil at 2.5 and 2.8 ns and with laser-smoothing techniques including DPP's, SSD, and DPR's. The saturation amplitude S is shown by the dashed line.

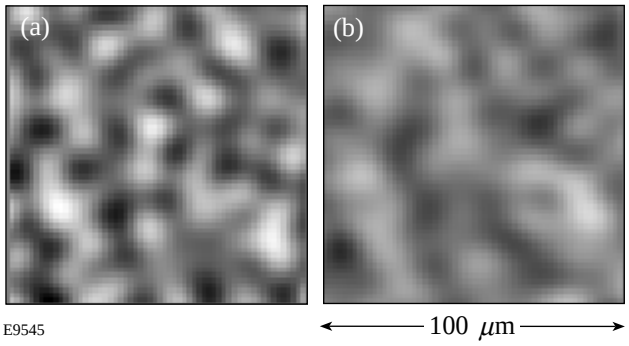

Figure 79.54
Late-time images of the target optical-depth perturbations captured at (a) 2.5 ns and (b) 2.8 ns with a 20-μm-thick target and with laser-smoothing techniques including DPP's, SSD, and DPR's.

and 2.8 ns (b). Compared to the image at 2.5 ns, features in the 2.8-ns image become much more round as neighboring bubbles coalesce, and the typical scale length of all the features becomes larger in the latter image. A 2-D model for bubble competition[17] predicts that such bubble coalescence occurs at higher bubble amplitudes and consequently much farther into the nonlinear regime than shown here. At the end of the drive (~3 ns) 1-D *LILAC* simulations predict an increase in ablation velocity (by a factor of 2) with the target decompressing quickly. In this case, target perturbations in optical depth could decrease because of the stabilizing effect of ablation.

Another possible explanation for the observed spectral behavior is that even earlier in the nonlinear regime (before the bubble coalescence), some short-scale-length bubbles move underneath larger, long-scale-length bubbles because larger bubbles grow faster than smaller bubbles.[17] The areal-density (or optical-depth) measurement becomes insensitive to short-scale-length bubbles because, in the direction of the x-ray propagation, the short-scale-length bubble becomes a part of the long-scale-length bubble, even though physically the two bubbles are still separate.

"Bowing" of the Target

Bowing of the target is another effect that has been observed and quantified in these experiments. Figure 79.55 schematically explains this effect. Before the shot, the CH target is attached to the massive Mylar washer. Without this washer a part of the laser energy from the laser beams, which irradiate the target at non-normal incidence, would miss the target and propagate toward opposing ports of the OMEGA target chamber, threatening to damage the laser system. During the drive, the central ~1-mm portion of a target accelerates, while the portion attached to the washer stays undriven. Toward the end of the drive the target becomes "stretched" (see Fig. 79.55). Experiments performed by Knauer[5] with the same drive condition on similar targets with preimposed 2-D corrugation showed that the wavelength of the corrugations increased 7% to 10% toward the end of the drive. This effect was explained by the target bowing and, as a result, stretching all features on the target, as though they were magnified.

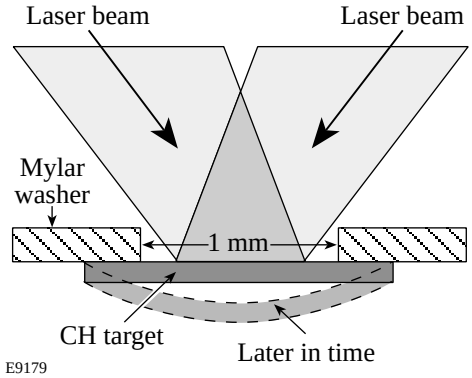

Figure 79.55
Schematic of the foil setup. The CH foil is attached to the massive Mylar washer. After the drive begins, it bows (dashed contour) because the drive pressure is applied only to its central part.

Figure 79.56 describes this effect quantitatively for one of the shots, using six target images of different time frames at 1.6, 1.9, 2.0, 2.2, 2.4, and 2.5 ns. It was assumed (for simplicity) that the main effect of the bowing was a magnification of late-time images with respect to early-time images. If so, the correlation of the magnified early-time image with late-time image should be higher than the correlation of the unmagnified images. (The bowing analysis was performed using raw, unfiltered target images because Wiener-filtered images were all processed with a fixed box size, not allowing this box size to vary, which is necessary to perform bowing analysis.) The dotted line in Fig. 79.56 shows the cross-correlation coefficient of the image at 2.2 ns with the image at 2.5 ns as the function of the magnification of the 2.2-ns image. The cross-correlation coefficient is maximized when the 2.2 ns image is magnified 1.04 times. To maximize the correlation of the same 2.2-ns image with the early-time image at 1.6 ns, it must be demagnified 0.97 times as shown by a dashed line in Fig. 79.56. The thick solid line shows the cross-correlation

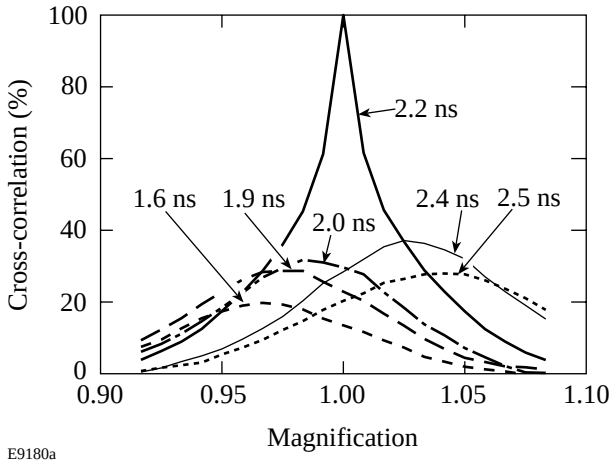

Figure 79.56
"Bowing" of the target. The cross-correlation of the image at 2.2 ns with the images at 2.5 ns, at 2.4 ns, itself, at 2.0 ns, at 1.9 ns, and at 1.6 ns as a function of the magnification of the 2.2-ns image. The smoothing techniques for this shot included DPP's, SSD, and DPR's.

coefficient of the image at 2.2 ns with itself. The shorter the time interval between images, the less magnification (or demagnification) is required for one of the images to be maximally correlated to the features in the other images. This analysis shows that as time progresses, the target images become magnified by about 7% to 10% between the 1.6-ns and 2.5-ns images. This effect is small enough to have minimal effect on the perturbation evolution. For example, Fig. 79.56 shows that all features of the 2.4-ns image are magnified by ~2.5% with respect to the earlier image at 2.2 ns. Figure 79.48(b) shows the spectral evolution for the same shot. The spectrum is peaked at ~34 mm^{-1} for the image at 2.2 ns, and the peak is shifted to ~20 mm^{-1} for the image at 2.4 ns. This ~40% change in the wavelength of the spectral peak has only a ~2.5% contribution from the bowing effect.

Finite Target Thickness Effect

The growth rates for 60-μm and 30-μm preimposed modulations, measured from 1.6 to 2.5 ns, are smaller by a factor of 2 to 2.5 than those measured for earlier times (from 0 to 1.2 ns) by Knauer[5] in similar experiments. These experiments used a larger initial amplitude of preimposed modulations (a_0 = 0.5 μm) and were driven with full smoothing techniques employed. This effect can be attributed to the perforation of the target by short-wavelength perturbations.

The short-wavelength perturbations imprinted by the laser beams are too small to be resolved in the experiments described in this article. Yet, they are estimated to evolve at late times to a σ_{rms} amplitude that equals about three to four (compressed and ablated) thicknesses of the target. If some bubbles penetrate the target, the mass available to feed the growth of the longer-wavelength preimposed modulations by lateral flow is limited; therefore, the growth of these modes is reduced.[15]

This effect has been studied numerically using calculations on the hydrocode *LEEOR2D*.[18] These simulations were conducted for conditions corresponding to the experiment with 20-μm-thick targets irradiated with five overlapped laser beams having various smoothing techniques and with various pulse shapes. One of the pulse shapes used was, as in the experiments, a 3-ns square with an exponential rise of 100 ps per decade and a peak intensity of 2×10^{14} W/cm^2.

Two levels of laser nonuniformity were simulated. The first, using DPP smoothed beams, had the same 1-D nonuniformity's power per mode as experimentally measured using 2-D time-integrated photographs of laser beams.[9] The second was of beams smoothed by DPP's, SSD and DPR's. The smoothing time of the SSD was 25 ps, approximately the effective smoothing time for the pulse used here.[34] Simulations using smooth laser beams were also performed.

2-D calculations of the perturbation evolution with an initial broadband spectrum of laser nonuniformities with and without preimposed 60- and 30-μm-wavelength, single-mode perturbations with initial amplitudes of 0.05 μm have been performed. For each case, the 2-D calculation with the preimposed modulation represents the direction of the preimposed modulation in the 3-D experiment, and the calculation without the preimposed modulation represents the perpendicular direction. The calculated amplitude of the preimposed mode was defined as the Fourier component of that mode in the latter calculation subtracted from that in the former calculation.

Even though the drive and smoothing conditions used in the simulations were similar to those used in the experiments described above, the comparison between the results of the 2-D simulations and the 3-D experiments must be considered only qualitatively because both the initial perturbations and the RT evolution are similar but not identical in 2-D and 3-D. Figure 79.57 shows the calculated evolution of the amplitude of the target areal density (normalized to the initial target density) of the preimposed 60- [Fig. 79.57(a)] and 30-μm-wavelength [Fig. 79.57(b)] modes for the three levels of laser nonuniformity described above. The amplitude of the preimposed modulations grows similarly for all cases until ~1.5 ns. After 1.5 ns, the amplitude of the preimposed mode continues to grow in the case of the smooth drive but is reduced

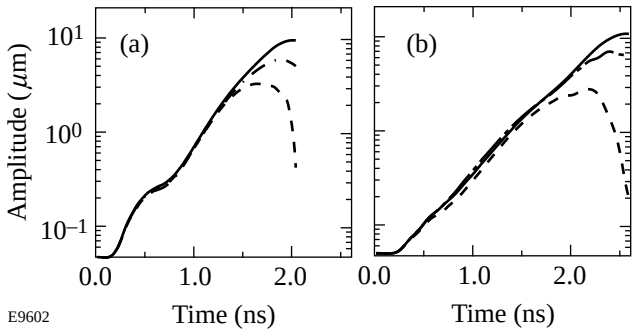

Figure 79.57
The evolution of the amplitude of the target areal density (normalized to the initial density) of preimposed (a) 30-μm- and (b) 60-μm-wavelength modes with smooth laser beams (solid), with DPP's, DPR's, and SSD (dash-dot), and with DPP's only (dashed) calculated using 2-D hydrodynamic simulations.

in the cases of the perturbed drives. This reduction is greater and starts earlier for the case of DPP only, without SSD and DPR's. This behavior is attributed to the perforation of the foil by the short-wavelength modes introduced by the laser nonuniformities.

This evolution can also be seen in Fig. 79.58, where the logarithmic growth rate of the areal-density perturbations of the preimposed modes $\left[\gamma = (\mathrm{d}a/\mathrm{d}t)/a\right]$ is plotted versus time. The growth rate decreases for both 60- [Fig. 79.58(a)] and 30-μm [(Fig. 79.58(b)] wavelengths of the preimposed mode due to the presence of the broadband spectrum of perturbations introduced by the laser nonuniformities.

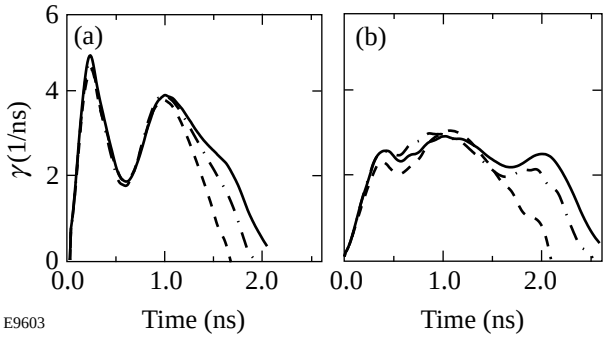

Figure 79.58
The evolution of the logarithmic growth rate $\left[\gamma = (\mathrm{d}a/\mathrm{d}t)/a\right]$ of the areal-density perturbations of (a) 30-μm and (b) 60-μm preimposed modes with smooth laser beams (solid), with DPP's, DPR's, and SSD (dash-dot), and with DPP's only (dashed).

The perforation of the target is most clearly seen in the density maps of the target, shown in Fig. 79.59 for the various 30-μm-wavelength calculations. It can be seen that the short-wavelength perturbations in the target perforate it at $t = 1.4$ ns for the case of DPP [Fig. 79.59(b)] and at $t = 1.6$ ns for the case of DPP's, SSD, and DPR's [Fig. 79.59(f)]. In the case of the uniform drive, the target is not yet perforated at these times, as can be seen in Fig. 79.60. When looking at later times, however, the perforation can clearly be seen to occur between $t = 1.8$ ns and $t = 2$ ns (Fig. 79.60).

One can clearly see the correlation between the times of perforation of the target in these density maps and the saturation in the growth of the preimposed modes, seen in Figs. 79.57 and 79.58. This correlation strengthens the explanation suggested above, that the growth of the preimposed modes is reduced when the broadband perturbations introduced by the laser nonuniformities perforate the target. The reason this reduction has not been measured in other experiments[5] is that the initial amplitude of the imposed perturbation in these experiments was larger; therefore, all measurements were performed at earlier times, when the imprinted perturbations had not yet evolved to large enough amplitudes and therefore the target was still not perforated.

To confirm that the saturation level and the late-time spectra do not depend on the target thickness, Fig. 79.61 shows the results of an additional experiment using a laser drive with DPP's only for 40-μm foil thickness. The measured spectra are shown for a 40-μm CH foil at 2.7 for one shot, and at 2.7 and 2.8 ns for the other shot. The saturation level was again calculated using the spectrally weighed attenuation length λ_x (which does not change significantly going from 20- to 40-μm foils) and the predicted compression (about 2 at ~2 to 3 ns). It can be seen that the finite target thickness does not affect the saturation level since the shapes of measured spectra are similar for both 20- and 40-μm target thicknesses, which is also in agreement with Haan's model. Note that the resulting

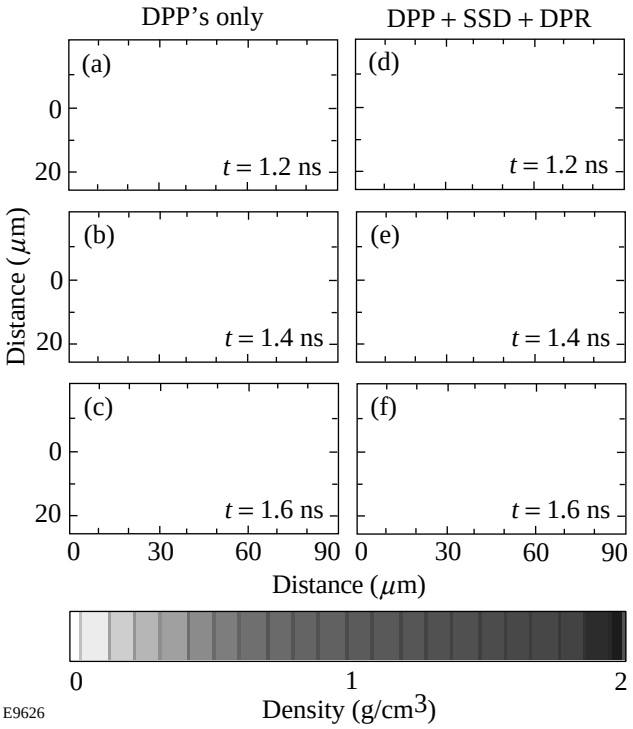

Figure 79.59
Density color maps of the target from the calculation with preimposed 30-μm mode driven by laser beams having DPP's only at (a) $t = 1.2$ ns, (b) $t = 1.4$ ns, (c) $t = 1.6$ ns, and by laser beams having DPP's, SSD, and DPR's at (d) $t = 1.2$ ns, (e) $t = 1.4$ ns, and (f) $t = 1.6$ ns.

acceleration of the 40-μm-thick foils was about a factor of 2 lower and the shock breakout time a factor of 2 later compared to 20-μm foils. The measured noise level is also about twice as high since approximately four-times-fewer photons are transmitted through the 40-μm foil. As a result, the imprint was detected only near the end of the drive and with DPP-only drive. When additional smoothing by SSD and DPR's were added, the initial imprinted amplitudes of target nonuniformity were small enough that, even at the end of the drive, no signal was measured above the noise.

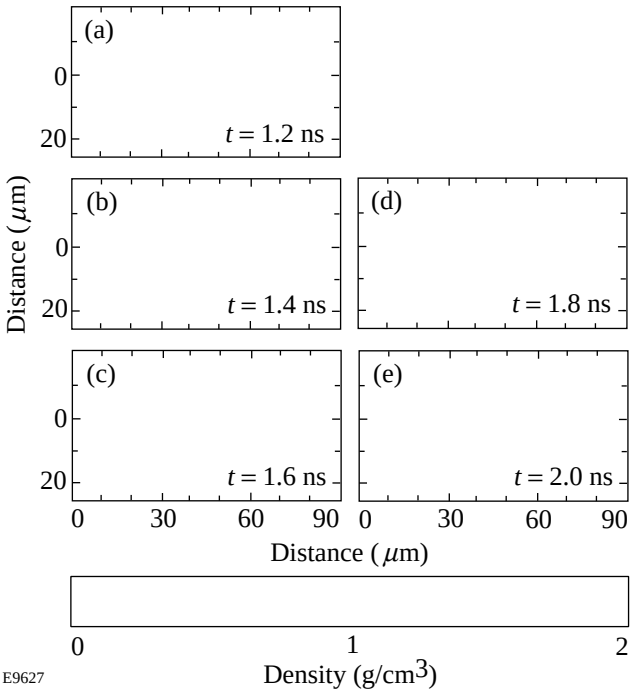

Figure 79.60
Density color maps of the target from the calculation with preimposed 30-μm mode driven by uniform laser beams at (a) t = 1.2 ns, (b) t = 1.4 ns, (c) t = 1.6 ns, (d) t = 1.8 ns, and (e) t = 2.0 ns.

Summary

This article has presented the measured evolution of 3-D broadband perturbations produced by laser imprinting in CH foils, accelerated by UV light. Using through-foil radiography these features were observed to saturate at levels in agreement with those predicted by Haan's model.[4] This behavior was noted in both the shape of the spatial Fourier spectra and in the temporal behavior of modes at various wavelengths. In addition, we noted that the growth of perturbations from broadband spectrum in the linear regime was the same as that for the linear growth of preimposed 2-D perturbations, also in agreement with the Haan model. These experiments were designed to test predicted saturation levels that are used in target designs for ICF experiments. We believe this is a clear experimental demonstration that the Haan model correctly predicts the saturation levels, spectral shape, and temporal evolution of broadband perturbations that are RT unstable. The contributions of measurement error and the effects of finite target thickness and target bowing have been shown to have little effect on our conclusions.

ACKNOWLEDGMENT

This work was supported by the U.S. Department of Energy Office of Inertial Confinement Fusion under Cooperative Agreement No. DE-FC03-92SF19460, the University of Rochester, and the New York State Energy Research and Development Authority. The support of DOE does not constitute an endorsement by DOE of the views expressed in this article.

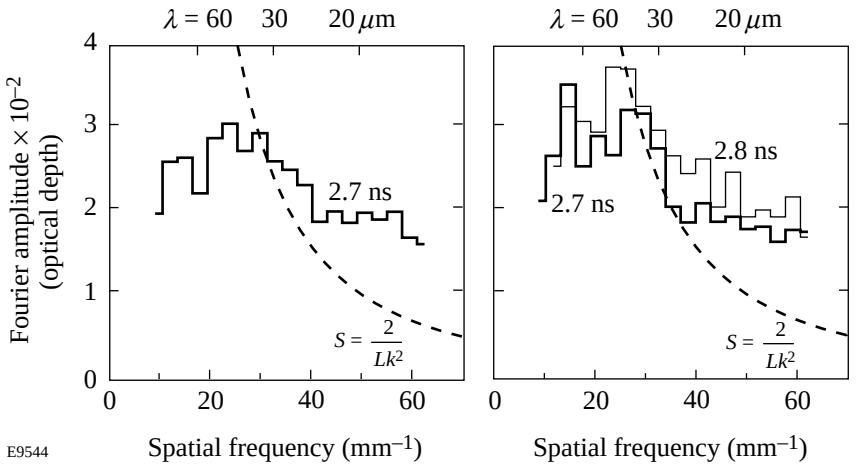

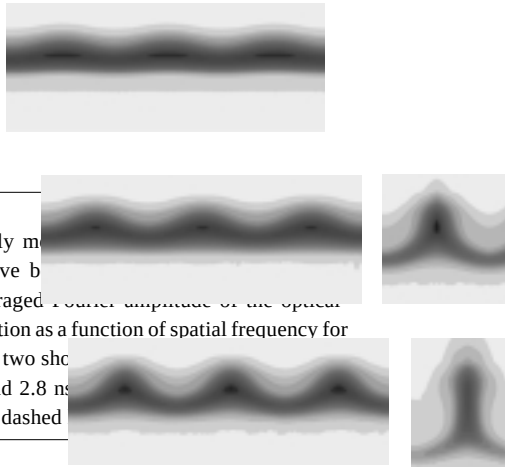

Figure 79.61
Experimentally m
DPP-only drive b
muthally averaged
depth modulation as a function of spatial frequency for
(a) one of the two sho
shot at 2.7 and 2.8 n
shown by the dashed

REFERENCES

1. D. K. Bradley, J. A. Delettrez, R. Epstein, R. P. J. Town, C. P. Verdon, B. Yaakobi, S. Regan, F. J. Marshall, T. R. Boehly, J. P. Knauer, D. D. Meyerhofer, V. A. Smalyuk, W. Seka, D. A. Haynes, Jr., M. Gunderson, G. Junkel, C. F. Hooper, Jr., P. M. Bell, T. J. Ognibene, and R. A. Lerche, Phys. Plasmas **5**, 1870 (1998).

2. S. E. Bodner, D. G. Colombant, J. H. Gardner, R. H. Lehmberg, S. P. Obenschain, L. Phillips, A. J. Schmitt, J. D. Sethian, R. L. McCrory, W. Seka, C. P. Verdon, J. P. Knauer, B. B. Afeyan, and H. T. Powell, Phys. Plasmas **5**, 1901 (1998).

3. S. V. Weber, S. G. Glendinning, D. H. Kalantar, M. H. Key, B. A. Remington, J. E. Rothenberg, E. Wolfrum, C. P. Verdon, and J. P. Knauer, Phys. Plasmas **4**, 1978 (1997).

4. S. W. Haan, Phys. Rev. A **39**, 5812 (1989).

5. J. P. Knauer, C. P. Verdon, D. D. Meyerhofer, T. R. Boehly, D. K. Bradley, V. A. Smalyuk, D. Ofer, P. W. McKenty, S. G. Glendinning, D. H. Kalantar, R. G. Watt, P. L. Gobby, O. Willi, and R. J. Taylor, in *Laser Interaction and Related Plasma Phenomena*, edited by G. H. Miley and E. M. Campbell (American Institute of Physics, New York, 1997), Vol. 406, pp. 284–293.

6. S. G. Glendinning, S. N. Dixit, B. A. Hammel, D. H. Kalantar, M. H. Key, J. D. Kilkenny, J. P. Knauer, D. M. Pennington, B. A. Remington, R. J. Wallace, and S. V. Weber, Phys. Rev. Lett. **78**, 3318 (1997).

7. K. Shigemori *et al.*, Phys. Rev. Lett. **78**, 250 (1997).

8. J. P. Knauer, R. Betti, D. K. Bradley, T. R. Boehly, T. J. B. Collins, V. N. Goncharov, P. W. McKenty, D. D. Meyerhofer, V. A. Smalyuk, C. P. Verdon, S. G. Glendinning, D. H. Kalantar, and R. G. Watt, "Single-Mode Rayleigh-Taylor Growth-Rate Measurements with the OMEGA Laser System," to be published in Physics of Plasmas.

9. T. R. Boehly, V. A. Smalyuk, D. D. Meyerhofer, J. P. Knauer, D. K. Bradley, C. P. Verdon, and D. Kalantar, in *Laser Interaction and Related Plasma Phenomena*, edited by G. H. Miley and E. M. Campbell (American Institute of Physics, New York, 1997), Vol. 406, pp. 122–129.

10. T. R. Boehly, V. A. Smalyuk, D. D. Meyerhofer, J. P. Knauer, D. K. Bradley, R. S. Craxton, M. J. Guardalben, S. Skupsky, and T. J. Kessler, J. Appl. Phys. **85**, 3444 (1999).

11. B. A. Remington *et al.*, Phys. Fluids B **5**, 2589 (1993).

12. R. J. Taylor *et al.*, Phys. Rev. Lett. **76**, 1643 (1996).

13. C. J. Pawley *et al.*, Phys. Plasmas **4**, 1969 (1997).

14. S. W. Haan, Phys. Fluids B **3**, 2349 (1991).

15. M. J. Dunning and S. W. Haan, Phys. Plasmas **2**, 1669 (1995).

16. J. P. Dahlburg *et al.*, Phys. Plasmas **2**, 2453 (1995).

17. D. Shvarts, U. Alon, D. Ofer, R. L. McCrory, and C. P. Verdon, Phys. Plasmas **2**, 2465 (1995).

18. D. Ofer, U. Alon, D. Shvarts, R. L. McCrory, and C. P. Verdon, Phys. Plasmas **3**, 3073 (1996).

19. M. M. Marinak *et al.*, Phys. Rev. Lett. **75**, 3677 (1995).

20. M. M. Marinak *et al.*, Phys. Rev. Lett. **80**, 4426 (1998).

21. V. A. Smalyuk, T. R. Boehly, D. K. Bradley, V. N. Goncharov, J. A. Delettrez, J. P. Knauer, D. D. Meyerhofer, D. Oron, and D. Shvarts, Phys. Rev. Lett. **81**, 5342 (1998).

22. T. R. Boehly, D. L. Brown, R. S. Craxton, R. L. Keck, J. P. Knauer, J. H. Kelly, T. J. Kessler, S. A. Kumpan, S. J. Loucks, S. A. Letzring, F. J. Marshall, R. L. McCrory, S. F. B. Morse, W. Seka, J. M. Soures, and C. P. Verdon, Opt. Commun. **133**, 495 (1997).

23. Y. Lin, T. J. Kessler, and G. N. Lawrence, Opt. Lett. **20**, 764 (1995).

24. S. Skupsky, R. W. Short, T. Kessler, R. S. Craxton, S. Letzring, and J. M. Soures, J. Appl. Phys. **66**, 3456 (1989).

25. S. G. Glendinning *et al.*, in *Applications of Laser Plasma Radiation II*, edited by M. C. Richardson and G. A. Kyrala (SPIE, Bellingham, WA, 1995), Vol. 2523, pp. 29–39.

26. V. A. Smalyuk, T. R. Boehly, D. K. Bradley, J. P. Knauer, and D. D. Meyerhofer, Rev. Sci. Instrum. **70**, 647 (1999).

27. T. Endo *et al.*, Phys. Rev. Lett. **74**, 3608 (1995).

28. R. Ishizaki and K. Nishihara, Phys. Rev. Lett. **78**, 1920 (1997).

29. B. A. Remington *et al.*, Phys. Fluids B **4**, 967 (1992).

30. M. C. Richardson, P. W. McKenty, F. J. Marshall, C. P. Verdon, J. M. Soures, R. L. McCrory, O. Barnouin, R. S. Craxton, J. Delettrez, R. J. Hutchison, P. A. Jaanimagi, R. Keck, T. Kessler, H. Kim, S. A. Letzring, D. M. Roback, W. Seka, S. Skupsky, B. Yaakobi, S. M. Lane, and S. Prussin, in *Laser Interaction and Related Plasma Phenomena*, edited by H. Hora and G. H. Miley (Plenum Press, New York, 1986), Vol. 7, pp. 421–448.

31. R. Betti, V. N. Goncharov, R. L. McCrory, and C. P. Verdon, Phys. Plasmas **5**, 1446 (1998).

32. H. Takabe, L. Montierth, and R. L. Morse, Phys. Fluids **26**, 2299 (1983).

33. H. Takabe *et al.*, Phys. Fluids **28**, 3676 (1985).

34. S. Skupsky, LLE, private communication (1998).